

Preparation and characterization of superhard AlB_2 -type WB_2 nanocomposite coatings

Chunlei Jiang, Zhiliang Pei, Yanming Liu, Jinquan Xiao, Jun Gong, and Chao Sun*

State Key Laboratory for Corrosion and Protection (SKLCP), Institute of Metal Research, Chinese Academy of Sciences, Shenyang 110016, P. R. China

Received 13 December 2012, revised 1 February 2013, accepted 12 February 2013

Published online 7 March 2013

Keywords hardness, magnetron sputtering, metastable phases, superhard coatings, WB_2

* Corresponding author: e-mail csun@imr.ac.cn, Phone: +86 024 8397 8081, Fax: +86 024 2389 1320

WB_2 nanocomposite coatings were synthesized by dc magnetron sputtering. The morphology, chemical composition, chemical bonding state, microstructure, hardness, and tribological properties were investigated. The columnar-structured coatings are dense and uniform. The as-deposited coatings were found to have a metastable AlB_2 -type structure as characterized by X-ray diffraction and further confirmed by high-resolution transmission electron microscopy. Coatings exhibit superhardness about 43.2 ± 5 GPa (taken from the

plateau region) obtained by nanoindentation. In addition, the steady-state friction coefficient $\mu = 0.23$ and wear rate $K = 6.5 \times 10^{-6} \text{ mm}^3 \text{ N}^{-1} \text{ m}^{-1}$ were obtained under dry sliding condition in ambient environments. These characteristics indicate AlB_2 -type WB_2 coatings have high potential application as superhard and low wear coatings. Moreover, the AlB_2 -type WB_2 can hardly be prepared using the conventional powder metallurgy technology without high pressure, and this study proposes a new practical approach to prepare it.

© 2013 WILEY-VCH Verlag GmbH & Co. KGaA, Weinheim

1 Introduction Recently, transition-metal borides have been extensively studied as superhard materials [1–8]. In particular, WB_2 has attracted our attention because of its excellent properties such as high value of hardness, chemical inertness, and electronic conductivity [9]. Two different crystal structures (i.e., AlB_2 -type and WB_2 -type) have been found experimentally for WB_2 phase. Interestingly, there has been a lot of research on WB_2 -type WB_2 [10–13], but only few reports of WB_2 with AlB_2 -type structure have been available. In 1966, AlB_2 -type WB_2 had been reported by Woods et al. [14], which was prepared by resistively heating an amorphous boron wire in a mixed atmosphere of WCl_6 and Ar at 800°C . Its crystal structure was assumed to crystallize in an AlB_2 -type structure (No. 191, $\text{P6}/\text{mmm}$, a , $b = 3.02 \pm 0.002 \text{ \AA}$, $c = 3.05 \pm 0.002 \text{ \AA}$) by comparing the X-ray data with those of other diborides (particularly, MoB_2 and MnB_2 , which have similar c/a ratios). The AlB_2 -type WB_2 prepared by this mentioned method was porous and could not be used to further investigate its basic properties. Additionally, the preparation process is not environmentally friendly due to its emission of toxic off-gas. Since that study, no preparation attempt was

reported until 2007 by Frotscher et al. [15], who tried but failed to synthesize the AlB_2 -type WB_2 phase using the powder metallurgy technique. On the basis of the first-principles calculations [16, 17], the AlB_2 -type WB_2 phase is only stable above 65 GPa. Therefore, it is difficult to prepare this metastable AlB_2 -type WB_2 phase using the conventional powder metallurgy technique without high-pressure conditions. Therefore, exploring a new, practical, and environmentally friendly way to synthesize this metastable AlB_2 -type WB_2 with good quality is significant not only for preparation and characterization of this kind of material but also for its further industrial applications.

The magnetron sputtering technique is believed to be the most promising method to prepare metastable compounds because of its effectiveness of vapor quenching, which is thought to arise from the suppression of the stable phases by freezing the atomic diffusion by reducing the solidification time [18]. In particular, some high-pressure phases needed to be fabricated under high-pressure condition can be easily formed using magnetron sputtering, such as NaCl-type AlN [19, 20]. Similarly, a predicated high-pressure phase, metastable AlB_2 -type WB_2 may also be synthesized by this

method. Also, the WB₂-type WB₂ compound is commercially available, which can be used as a target. Moreover, using compound targets to deposit films can generate environmental benefits by avoiding the use of toxic resource gases such as borane as precursor materials. Therefore, in this paper, we attempt to synthesize AlB₂-type WB₂ coatings using dc magnetron sputtering, and investigate their morphology, microstructure, chemical composition, and bonding state as well as mechanical properties (including hardness, frictional, and wear properties).

2 Experimental

2.1 Synthesis of WB₂ coatings WB₂ coatings were deposited by dc magnetron sputtering. The schematic diagram of the experimental setup is shown in Fig. 1. One water-cooled rectangular planar target (WB₂-type WB₂ bulk with 99.5% purity and 270 mm × 70 mm × 7 mm in size) was mounted in the sputtering system. 304 stainless steel slices were used as the substrates. Before the deposition, the substrates were polished, ultrasonically cleaned in acetone and ethanol, dried and then mounted onto the heater opposing the target. The deposition process was conducted following a three-step procedure. (i) The heater began to be resistively heated to 680 °C when a vacuum below 5×10^{-3} Pa was achieved. (ii) The chamber was backfilled with argon to 0.9 Pa when the base pressure came to about 2.0×10^{-3} Pa, and then the substrate was further *in situ* cleaned by argon ion etching with a substrate bias of −180 V for 15 min. (iii) The deposition was performed with an argon partial pressure of 0.3 Pa and a substrate bias of −150 V for 2 h. During the whole process the target-to-substrate distance, substrate temperature and target power were maintained at 50 mm, 680 °C and 195 W, respectively.

2.2 Characterization of morphology Scanning electron microscopy (SEM; S-3400N, Hitachi, Japan) was carried out to characterize the morphology of the coatings. An atomic force microscope (AFM; Pico Scan 2500, Agilent Technologies, USA) was also used to capture the surface

images. A commercially available silicon tip was used and the microscope was run in a “tapping mode.”

2.3 Composition and bonding-state analysis

The composition was analyzed by an electron probe X-ray microanalyzer (EPMA; EPMA-1600, Shimadzu, Japan) with WB₂-type WB₂ as the calibration standard sample. Chemical bonding state was investigated by X-ray photoelectron spectroscopy (XPS; ESCALAB250, Thermo-VG Scientific, USA).

2.4 Microstructure analysis X-ray diffraction (XRD; D/Max 2500PC, Rigaku, Japan) was used to identify the phase and analyze the crystal structure. According to the lattice constants and the crystal structures reported by Woods et al. [14], the diffraction patterns of AlB₂-type WB₂ phase has been simulated on the Cerius² workstation. To calculate the lattice constants, the coatings were separated from the stainless steel substrates, and then ground into powders. Subsequently, the powders were vacuum-annealed at 800 °C for an hour to relax the stress. The diffraction profiles were measured in the step-scan model with a step size of 0.02° and a counting time of 8 s per step. High-resolution transmission electron microscopy (HRTEM; JEM-2100F, JEOL, Japan) was also performed to investigate the microstructure.

2.5 Evaluation of mechanical properties The hardness was evaluated using a nanoindenter (Nano indenter G200, Agilent Technologies, USA) with a Berkovich indenter tip. The continuous stiffness mode (CSM) was employed and ten indentations for every sample coating were made during our measurement.

A ball-on-disk tribometer (MS-T3000) was used to test its friction and wear properties at room temperature in ambient air at RH = 40%. The Al₂O₃ ball (Ø = 4 mm) was used with a constant normal load of 1.96 N. A sliding speed of 0.084 m s^{−1} and sliding distance of 300 m was used in the experiments and the friction coefficient (μ) was continuously recorded during the testing. The wear volume of the coating, V , was calculated as

$$V = 2\pi rA, \quad (1)$$

where r is the radius of the wear track and A is the cross-sectional area of the wear track measured by a surface profiler (Alpha-Step IQ; KLA Tencor).

The wear rate K was calculated using the following equation:

$$K = \frac{V}{SF_N}, \quad (2)$$

where V is the wear volume, S is the sliding distance and F_N is the normal load. The wear morphology and surface roughness of the coating were investigated using a surface mapping microscope (Micro XAM; KLA Tencor). The surface roughness is of great importance in the tribosystem since it will affect the friction and wear

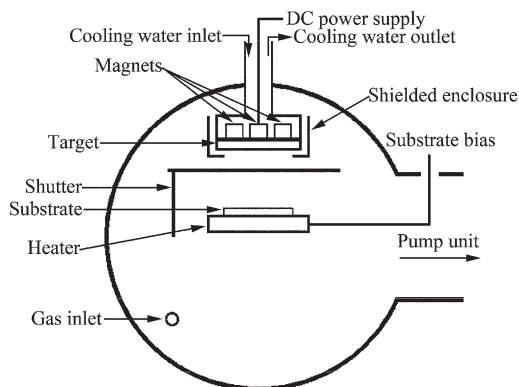


Figure 1 Schematic drawing of the dc magnetron sputtering system.

characteristics. In this work, the surface roughness was characterized using the average roughness R_a (arithmetic average of absolute values). The roughness of the coating $R_{a(c)}$, and the wear track $R_{a(t)}$ in the sliding direction were measured.

3 Results and discussion

3.1 Morphology Figure 2 shows the SEM images of the as-deposited coatings. The plan view of the coating is presented in Fig. 2a, evidencing a dense and uniform coating surface. The morphology of the cross-section is characterized by a compact columnar structure, as illustrated in Fig. 2b. In addition, the thickness of the as-deposited coating is found to be about $2.8\ \mu\text{m}$ with a deposition rate of $23\ \text{nm min}^{-1}$. As illustrated in Fig. 3a and b, the grain morphology displays a spindle-like shape. The average width and length of these spindles were found to be about 60 and 200 nm, respectively. And the aspect ratio (length/width) of these grains was about 3.3. This suggests that the particles forming the coatings have higher growth rate in one particular lateral direction than in the height direction. The surface roughness R_q (root mean squared) was also determined at about $57.5\ \text{\AA}$, indicating a very smooth surface.

3.2 Composition and bonding state The sample coating was sputter cleaned for 780 s before the XPS analysis to remove the contamination layer of hydrocarbons and oxidation products. Figure 4a shows a typical XPS survey spectrum from the sample coatings. Only W and B elements were observed. While in the EPMA survey spectrum, as shown in Fig. 4b, besides the W and B elements, O, C, and Ar elements were also observed. C and O impurities are unavoidable because the sample coating was not sputter cleaned before the EPMA analysis to remove the adsorbed hydrocarbon and oxidation layers. The presence of a very small amount of Ar is caused by the incorporation due to the basic Ar pressure during coating deposition. XPS analysis gave the composition W/B as about 1:1.13, which is far from stoichiometric. This is because XPS is a semiquantitative technique for surface chemical analysis. In case of EPMA, WB_2 -type WB_2 with similar crystal structure and composition to AlB_2 -type WB_2 was used as the calibration standard

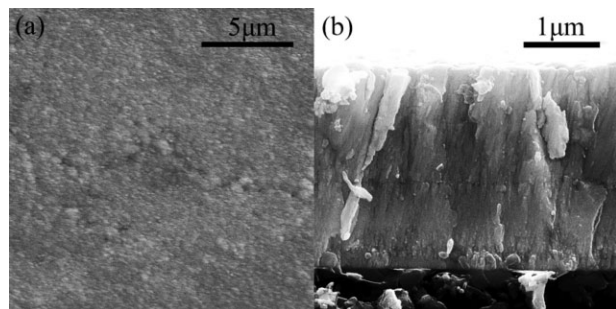


Figure 2 SEM images of the as-deposited coatings: (a) plan view; (b) cross-sectional view.

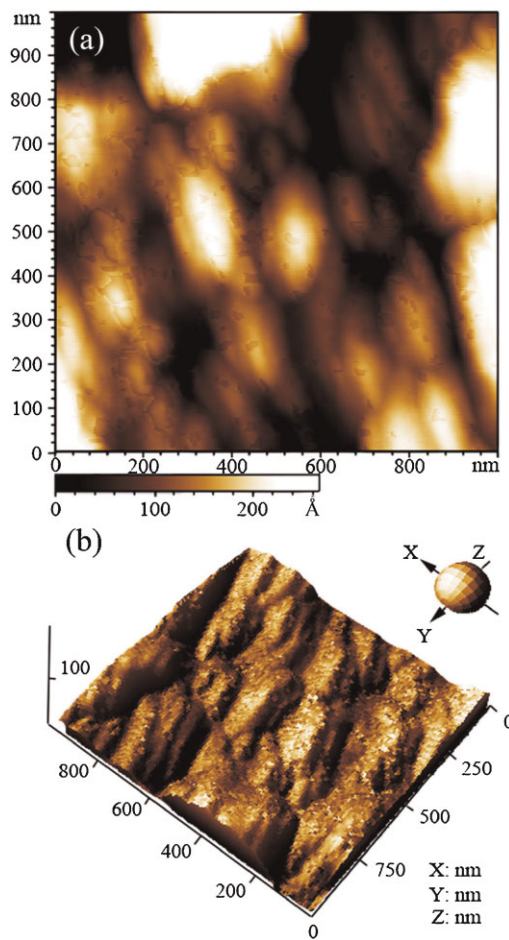


Figure 3 AFM images of the as-deposited coatings. (a) 2D view, (b) 3D view. The scan size is $1\ \mu\text{m} \times 1\ \mu\text{m}$.

sample, and the coating chemistry was found to contain about 35 at.% W and 65 at.% B. And the W/B atomic ratio is about 1:1.9, which is close to 1:2.

To determine the chemical state of W and B, the binding energies were calibrated by the C_{1s} peak at 284.6 eV. Figure 5 illustrates the XPS spectra of W 4f and B 1s after being sputter cleaned for 780 s. As shown in Fig. 5a, W 4f exhibits a double peak for W $4f_{7/2}$ and W $4f_{5/2}$ spectra: one at 31.25 eV and the other at 33.4 eV. The double peak is considered to be connected with the W–B bonding, since a shift to the higher-energy side was found compared with that of pure W (centered at 31 eV and 33.15 eV) [21], reflecting a charge transfer from tungsten to boron during the process of bonding. Additionally, as presented in Fig. 5b, the B 1s peak is centered at 188.1 eV, which is equal to that of MoB_2 (188.1 eV) and close to AlB_2 (188.2 eV) [21], indicating the chemical bonding state of boron is similar to that in MoB_2 and AlB_2 . Therefore, combining the preceding composition analysis, the obtained tungsten boride is most likely to crystallize as AlB_2 -type WB_2 with the same crystal structure as that of MoB_2 and AlB_2 . To test this assumption, XRD analysis was carried out as below.

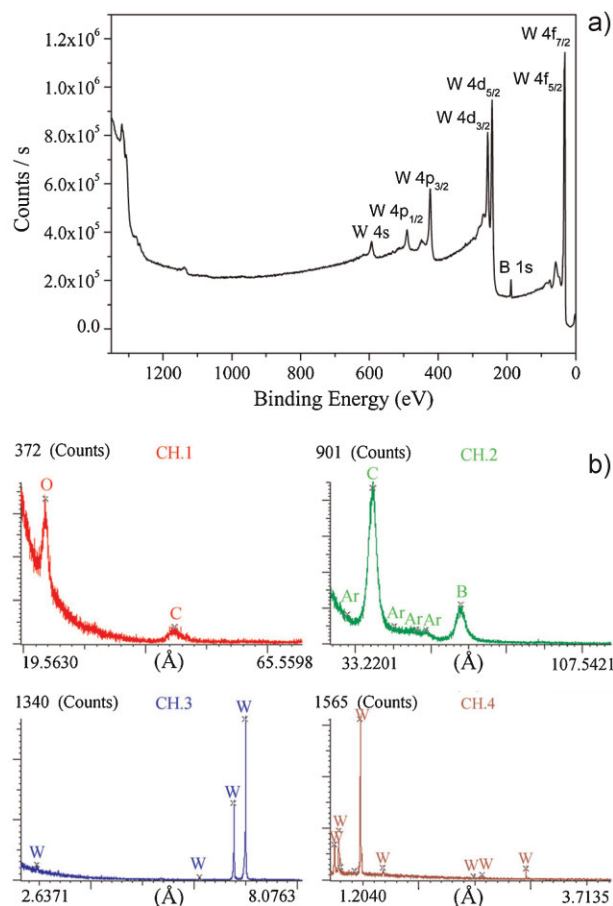


Figure 4 (a) XPS survey spectrum after being sputter cleaned for 780 s and (b) EPMA survey spectrum of the as-deposited coatings.

3.3 Microstructure Figure 6a and b represents experimental curve of this work and the simulated curve from Woods et al.'s data [14], respectively. It is noted that the simulated curve (b) is in full accordance with the diffraction data (the dotted line in Fig. 6) reported by Woods et al. [14], revealing the credibility of our currently simulated results. The diffraction peaks in the current experimental curve (a) are in good agreement with those in the simulated curve (b), indicate that the as-deposited coating belongs to the AlB₂-type WB₂ phase. Diffraction-peak broadening was also observed in the current experimental profile, which can be attributed to the small grain size or the imperfect crystal structure. In addition, three weak diffraction peaks of the 304 stainless steel substrate emerged in the diffraction pattern (b). Note that no other W–B phases were detected. Therefore, in contrast to Liang et al.' report [22], our work has demonstrated the possibility of making AlB₂-type WB₂.

The crystallite size of the coatings from the XRD pattern was calculated using the Debye–Scherrer formula

$$D = \frac{0.9\lambda}{\beta \cos \theta},$$

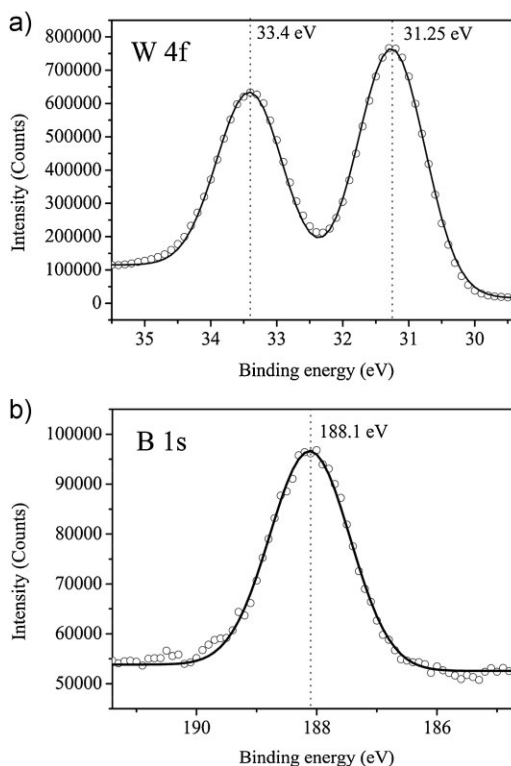


Figure 5 High-resolution XPS scan spectra over (a) W 4f and (b) B 1s of the sample coating after being sputter cleaned for 780 s.

where D is the crystallite size of the coatings, λ is the wavelength of Cu K α line, β is the FWHM in radians, and θ is the Bragg angle. Low-angle diffraction peaks (001), (100), and (101) were used to calculate the crystallite size. An average crystallite size of 21.2 ± 0.2 nm was obtained. This value of crystallite size is considerably smaller than the

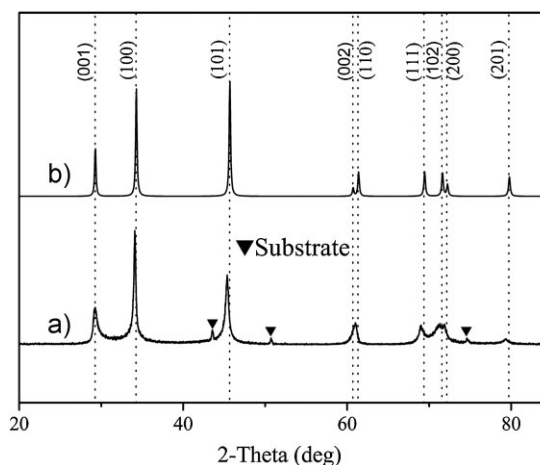


Figure 6 X-ray diffraction spectra: (a) current experimental curve, (b) simulated curve from the reported lattice constants of Woods et al. [14]. The dotted lines refer to the experimental diffraction data from Woods et al. [14]. Filled triangles represent the diffraction peaks of the 304 stainless steel substrate.

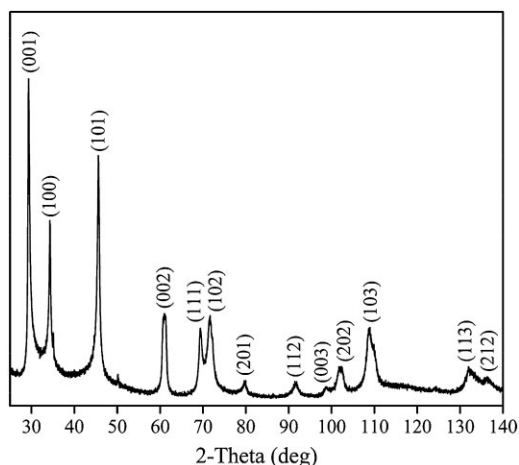


Figure 7 X-ray diffraction pattern of the AlB₂-type WB₂ powders vacuum annealed at 800 °C for an hour.

grain size observed from the AFM measurement. The discrepancy is mostly due to the fact that the internal stress and defects also contribute to the XRD peak broadening, and the mean crystallite size estimated by this method is normally smaller than the actual value.

Figure 7 shows the X-ray diffraction pattern of the vacuum-annealed AlB₂-type WB₂ powders. Lattice constants were calculated using high-angle diffraction peaks (201) and (112). The derived lattice constants of $a = 3.02 \pm 0.003$ Å and $c = 3.06 \pm 0.007$ Å agree well with the values reported by Woods et al. [14].

HRTEM images of the as-deposited coatings are shown in Fig. 8a–c and fast Fourier transform (FFT) patterns derived from the corresponding HRTEM images are illustrated in the inset of Fig. 8a and b, which are indexed as $[1\bar{2}10]$ and $[1\bar{2}13]$, respectively. These FFT patterns are also informative for determining the crystal structure. The inset images of Fig. 8a and b show the presence of both the (0001) and (11 $\bar{2}$ 1) reflections, which is exactly coincident with the XRD results. Figure 8c illustrates the microstructure of the coatings. The black-cycled regions display a typical maze-like pattern, which is expected from the amorphous structure [23]. This was further confirmed by the FFT pattern of the black-cycle region as presented in Fig. 8d, which exhibits a typical amorphous halo characteristic. Therefore, the coatings were not fully crystallized and considered to be a nanocomposite made up of the AlB₂-type WB₂ crystalline phase and an amorphous phase. As characterized by AFM, the spindle-like grain structure was also observed in the plan-view bright-field image of the sample coating (Fig. 9). And the average grain size is also in accordance with the AFM analysis. Additionally, small grain size and imperfect crystal structure also explain the X-ray diffraction peaks broadening.

3.4 Mechanical properties

Figure 10 illustrates the hardness–displacement curve of the sample coatings and the load–displacement curves are presented in the inset image of

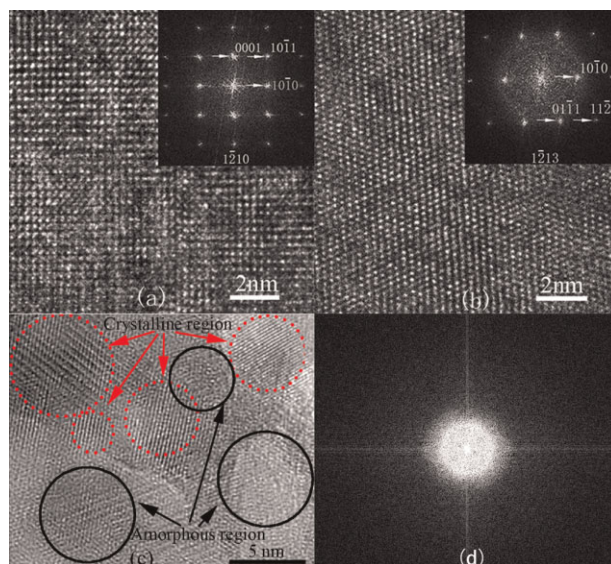


Figure 8 HRTEM and FFT patterns of the as-deposited coating. Figures (a), (b), and (c) are HRTEM images, and the inset figures of (a) and (b) are FFT patterns indexed as $[1\bar{2}10]$ and $[1\bar{2}13]$, which are derived from the corresponding HRTEM images. Figure (d) shows the FFT pattern of the amorphous region.

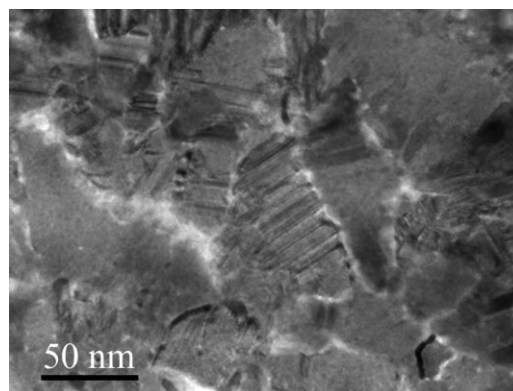


Figure 9 Plan-view bright-field image of the as-deposited coating.

Fig. 10. As observed in the inset figure, the loading and unloading curves of ten indentations almost overlap with each other, showing highly reliable indentation results and repeatable deformation behavior of the coatings. At small indentation depths (0–60 nm), the hardness increases with increasing depth. Then, the hardness shows a slight decrease and then reaches a plateau in the range of 130–180 nm. Next, the hardness begins to decrease with increasing indentation depth; and this is due to the well-known indentation size effect (ISE). Although many models have been developed to explain this effect, strain gradient plasticity is the most frequently used one [24]. In this work, hardness values were chosen at two different penetration depths, one at the plateau region and the other at 400 nm indentation depth. The two average hardness values are 49.8 ± 3.6 GPa and

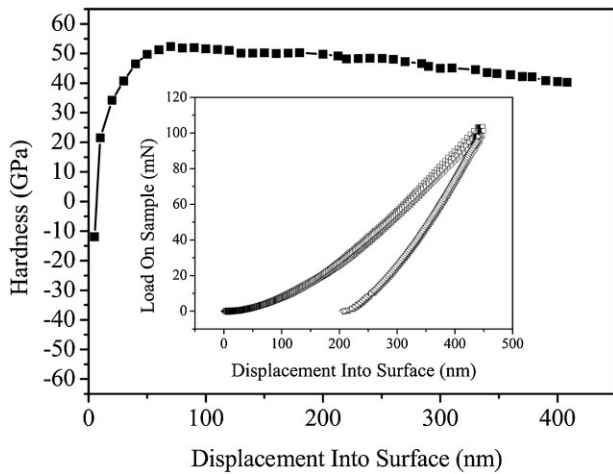


Figure 10 Hardness of the as-deposited coatings plotted as a function of indentation depth. The inset figure shows the load–displacement curves of ten indentations.

40.5 ± 1.6 GPa. The high hardness might be related to the nanocomposite structure [25] as observed in the TEM analysis. After many measurements on sample coatings deposited on the same condition, the two mean hardness values were 43.2 ± 5 GPa and 34.6 ± 2.7 GPa. The difference in the hardness values might be caused by the variations of the processing parameters during the deposition process, such as target voltage, target current, bias voltage, argon partial pressure, and so on.

The time-dependent behavior of friction was divided into four stages as shown in Fig. 11. Stage I displays a short running-in phase followed by a steady-state phase, i.e., stage II, with an average friction coefficient value $\mu \approx 0.28$. And in this early stage of dynamic friction the coefficient of friction is largely controlled by behavior contact between hard asperities on behavior WB₂ coating and behavior Al₂O₃ ball. In stage III, the friction coefficient begins to decrease and then enters into another steady-state phase lasting about 10 min with a low friction coefficient $\mu \approx 0.23$. The decrease

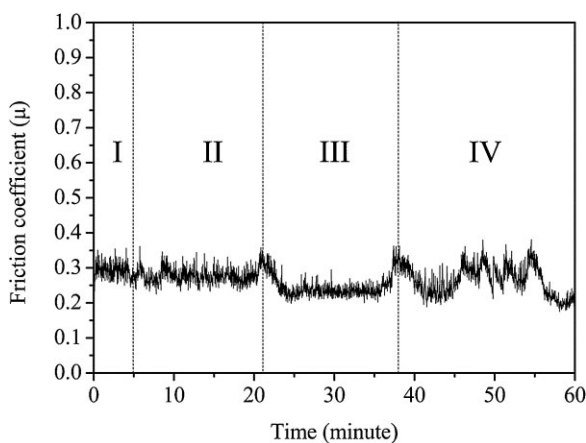


Figure 11 Friction coefficient of the as-deposited coating in sliding contact with Al₂O₃ ball.

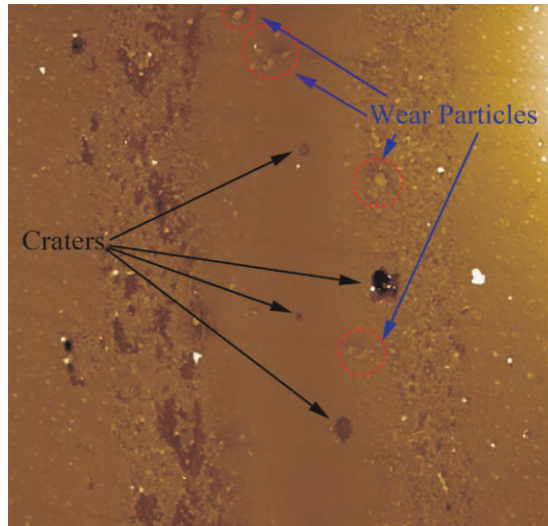


Figure 12 Surface morphology of the wear track.

of the friction coefficient might be due to the reduction of the surface roughness, since after a period of sliding the asperities will be removed and the surface will be getting smoother, resulting in a low friction coefficient. This can be confirmed by the surface roughness measurement. The roughness of the wear track $R_{a(t)} = 12$ nm is much smaller than the roughness of the coating $R_{a(c)} = 26.5$ nm. Note that the friction coefficient value fluctuates very violently in the last stage of the friction process. A possible explanation for such fluctuations in the friction coefficient values can be suggested as follows. Due to the repeated traversals for a long time, crack initiation and propagation will occur. Propagating to a certain degree, the cracks will fracture and wear particles will be generated by delamination. As the wear particles are entrapped between the sliding surfaces, the moving parts will be hindered, leading to high friction values. As the wear particles leave the interface, the friction coefficient tends to low values. As seen in Fig. 12, cracks, wear particles and craters caused by the creation of the delamination wear particles are observed. Additionally, the wear rate K is about $6.5 \times 10^{-6} \text{ mm}^3 \text{ N}^{-1} \text{ m}^{-1}$ calculated on basis of Eqs. (1) and (2).

4 Conclusions This work has demonstrated a new practical and environmentally friendly strategy for fabricating the metastable AlB₂-type WB₂ phase, which can hardly be prepared using the conventional powder metallurgy technology without high pressure. The morphological observations showed that the coatings were dense and uniform with columnar structure. The XRD and HRTEM analysis showed that the WB₂ coatings had a metastable AlB₂-type structure. The as-deposited coatings were found to possess a nanocomposite structure exhibiting a superhardness about 43.2 ± 5 GPa (taken from the plateau region). During the sliding process, the steady-state friction coefficient value is about 0.23. Additionally, the wear rate is

about $6.5 \times 10^{-6} \text{ mm}^3 \text{ N}^{-1} \text{ m}^{-1}$. These characteristics indicate that AlB₂-type WB₂ coatings have high potential application as superhard and low-wear coatings.

Acknowledgements This work was supported by the National Key Basic Research Program of China (973 Program, No. 2012CB625102). The authors would like to thank Prof. Dr. Xingqiu Chen and Prof. Dr. Hao Lei for their helpful discussions.

References

- [1] R. B. Kaner, J. J. Gilman, and S. H. Tolbert, *Science* **308**, 1268–1269 (2005).
- [2] H. Y. Chung, M. B. Weinberger, J. B. Levine, A. Kavner, J. M. Yang, S. H. Tolbert, and R. B. Kaner, *Science* **316**, 436–439 (2007).
- [3] J. B. Levine, S. L. Nguyen, H. I. Rasool, J. A. Wright, S. E. Brown, and R. B. Kaner, *J. Am. Chem. Soc.* **130**, 16953–16958 (2008).
- [4] S. N. Tkachev, J. B. Levine, A. Kisliuk, A. P. Sokolov, S. Q. Guo, J. T. Eng, and R. B. Kaner, *Adv. Mater.* **21**, 4284–4286 (2009).
- [5] J. B. Levine, S. H. Tolbert, and R. B. Kaner, *Adv. Funct. Mater.* **19**, 3519–3533 (2009).
- [6] J. B. Levine, J. B. Betts, J. D. Garrett, S. Q. Guo, J. T. Eng, A. Migliori, and R. B. Kaner, *Acta Mater.* **58**, 1530–1535 (2010).
- [7] R. Mohammadi, A. T. Lech, M. Xie, B. E. Weaver, M. T. Yeung, S. H. Tolbert, and R. B. Kaner, *Proc. Natl. Acad. Sci. USA* **108**, 10958–10962 (2011).
- [8] R. Mohammadi, M. Xie, A. T. Lech, C. L. Turner, A. Kavner, S. H. Tolbert, and R. B. Kaner, *J. Am. Chem. Soc.* **134**, 20660–20668 (2012).
- [9] G. V. Samsonov and I. M. Vinitskii, *Handbook of Compounds* (IFI/Plenum, New York, 1980), p. 40, 143, and 184.
- [10] T. Lundström, *Ark. Kem.* **30**, 115–127 (1968).
- [11] X. F. Hao, Y. H. Xu, Z. J. Wu, D. F. Zhou, X. J. Liu, X. Q. Cao, and J. Meng, *Phys. Rev. B* **74**, 224112 (2006).
- [12] Q. F. Gu, G. Krauss, and W. Steurer, *Adv. Mater.* **20**, 3620–3626 (2008).
- [13] J. V. Rau, A. Latini, R. Teghil, A. D. Bonis, M. Fosca, R. Caminiti, and V. R. Albertini, *ACS Appl. Mater. Interfaces* **3**, 3738–3743 (2011).
- [14] H. P. Woods, F. E. Wawner, and B. G. Fox, *Science* **151**, 75 (1966).
- [15] M. Frotscher, W. Klein, J. Bauer, C. M. Fang, J. F. Halet, A. Senyshyn, C. Baetz, and B. Albert, *Z. Anorg. Allg. Chem.* **633**, 2626–2630 (2007).
- [16] E. Zhao, J. Meng, Y. M. Ma, and Z. J. Wu, *Phys. Chem. Chem. Phys.* **12**, 13158–13165 (2010).
- [17] X.-Q. Chen, C. L. Fu, M. Krčmar, and G. S. Painter, *Phys. Rev. Lett.* **100**, 196403-1 (2008).
- [18] T. Ogushi, K. Nishi, H. Nagai, and T. Numata, *J. Low-Temp. Phys.* **41**, 13–23 (1980).
- [19] M. Ueno, A. Onodera, O. Shimomura, and K. Takemura, *Phys. Rev. B* **45**, 10123 (1992).
- [20] A. Sugishima, H. Kajioka, and Y. Makino, *Surf. Coat. Technol.* **97**, 590–594 (1997).
- [21] C. D. Wagner, W. M. Riggs, L. E. Davis, J. F. Moulder, and G. E. Mulinberg, *Handbook of X-ray Photoelectron Spectroscopy* (Perkin-Elmer Corporation, Minnesota, 1979).
- [22] Y. C. Liang, X. Yuan, and W. Q. Zhang, *Phys. Rev. B* **83**, 220102(R) (2011).
- [23] C. Fan, D. V. Louzguine, C. F. Li, and A. Inoue, *Appl. Phys. Lett.* **75**, 19 (1999).
- [24] H. Gao, Y. Huang, and W. D. Nix, *Naturwissenschaften* **86**, 507 (1999).
- [25] S. Zhang, D. Sun, Y. Fu, and H. Du, *Surf. Coat. Technol.* **167**, 113–119 (2003).